High-Frequency Behavior of Graphene-Based Interconnects—Part I: Impedance Modeling

Deblina Sarkar, *Student Member, IEEE*, Chuan Xu, *Student Member, IEEE*, Hong Li, *Student Member, IEEE*, and Kaustav Banerjee, *Senior Member, IEEE*

***Abstract*—This paper presents the first detailed methodology for the accurate evaluation of high-frequency impedance of graphene-based structures relevant to on-chip interconnect and inductor applications. Going beyond the simplifying assumptions of Ohm's law, the effects of electric-field variation within a mean free path and current dependency on the nonlocal electric-field are taken into account to accurately capture the high-frequency behavior of graphene ribbons (GRs). At the same time, a simplified approach that may be adopted at lower frequencies is also explained. Starting from the basic Boltzmann equation and combining with the unique dispersion relation for graphene in its hexagonal Brillouin zone, the current density across the GR structure is derived. First, a semi-infinite slab of GR is analyzed using the theory of Fourier integrals, which is followed by the development of a rigorous methodology for practical finite structures based on a self-consistent numerical calculation of the derived current density using the Green's function approach.**

***Index Terms*—Anomalous skin effect (ASE), carbon nanomaterials, graphene, high frequency, impedance, intercalation doping, interconnects, skin effect, specularity.**

I. Introduction

GRAPHENE is considered a potential material for very large-scale integration (VLSI) interconnects [1]–[4] due to its unique properties, e.g., capability to conduct high current densities, high thermal conductivity [5], and long mean free path (MFP), which leads to large electrical conductance [6]. The detailed modeling of low-frequency conductance and delay analysis of graphene ribbons (GRs) have already been reported in a previous work [1]. As a prospective interconnect material, apart from performance analysis in terms of dc conductance and delay, a thorough investigation of the high-frequency effects of GRs is equally compelling. Note that the significant frequency is already $>$ 60 GHz for the 45-nm technology [7]. Recently, it has been shown that carbon nanotubes (CNTs) can be very attractive for high-frequency applications such as on-chip inductor design due to their large momentum relaxation time [8]. GRs not only enjoy a large momentum relaxation time but also are more controllable from the fabrication point of view due to their planar structure. Thus, detailed analysis of the high-frequency behavior of GRs is highly desirable, and accurate modeling of the intricate processes occurring at high frequencies in GR is of absolute necessity.

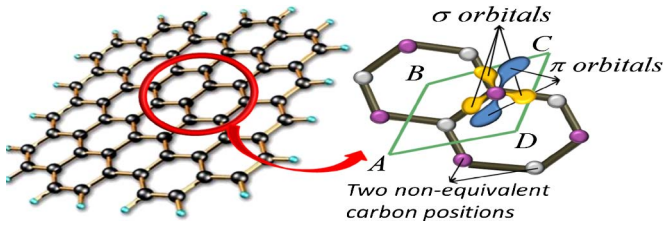

Fig. 1. Basic honeycomb structure of graphene. Graphene has two non-equivalent carbon positions. ABCD represents the unit cell, which contains the two types of atoms. The three in-plane σ orbitals (constructed from the $2s$, $2p_x$, and $2p_y$ valence orbitals) and the π orbital (associated with the overlap of the $2p_z$ valence orbitals) perpendicular to the sheet are shown for one of the carbon atoms. The π orbitals determine the conduction properties of graphene.

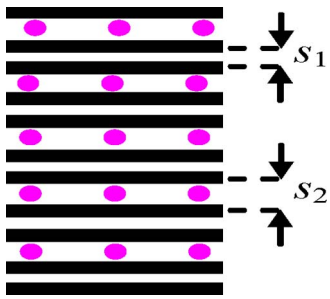

Fig. 2. Schematic of a stage-2 intercalation doped multilayer GR. The solid lines indicate graphene layers, whereas the dots indicate intercalation dopant layers. s_1 and s_2 are the layer spacing between two adjacent graphene layers.

II. Issues in High-Frequency Behavior of GR

The basic structure and orbitals of graphene are shown in Fig. 1. Graphene can be either monolayered or multilayered (doped or undoped). The focus of this paper will be on doped multilayer GRs, which are interesting for practical high-frequency applications such as interconnect and inductor design. The monolayer and undoped multilayer GRs have very high resistivity and are not of much interest for such applications [1]. The stage-2 AsF_5 intercalated GR (see Fig. 2) has been shown to have in-plane conductivity greater than that of Cu [1], [9], and hence, it is chosen as a representative case of doped GRs. Nevertheless, our methodology is also applicable to any other type of doping.

Manuscript received April 23, 2010; revised October 5, 2010; accepted December 1, 2010. Date of current version February 24, 2011. This work was supported in part by the National Science Foundation under Grant CCF-0811880. The review of this paper was arranged by Editor M. A. Reed.

The authors are with the Department of Electrical and Computer Engineering, University of California–Santa Barbara, Santa Barbara, CA 93106-9560 USA (e-mail: deblina@ece.ucsb.edu; chuanxu@ece.ucsb.edu; hongli@ece.ucsb.edu; kaustav@ece.ucsb.edu).

Color versions of one or more of the figures in this paper are available online at http://ieeexplore.ieee.org.

Digital Object Identifier 10.1109/TED.2010.2102031

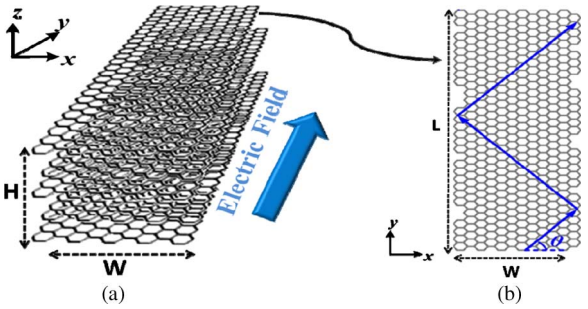

Fig. 3. (a) Multilayer GR structure showing the selection of axis and the direction of electric field. (b) Carrier transport elaborated on a single layer. The carrier transport in GR is confined within each 2-D layer. The interlayer transport is negligible. Thus, carriers can only move in the x- and y-directions, get scattered by the edges, and finally contribute to the current along y.

A. ASE and Ohm's Law

The high-frequency effects in doped multilayer GRs, as shown in Fig. 2 [1], are very complicated and require serious consideration of various intricate processes as described in the following discussion. For high-frequency investigation, each GR layer cannot be treated as a single element with uniform electric field and current because of the current density redistribution within a GR layer due to the skin effect. Moreover, because of its large MFP, GR is susceptible to the anomalous skin effect (ASE). ASE occurs when the MFP becomes comparable to the skin depth [10]. When the MFP is much smaller compared to the skin depth, an electric field can be assumed to be constant within the MFP. This case results in current density being directly proportional to the electric field, with the constant of proportionality being the conductivity, and thus, the Ohm's law is satisfied. However, when the skin depth becomes comparable to the MFP, the carriers can no longer be considered to be moving under the influence of a constant field between collisions, and the current at any point will also be influenced by values of the electric field at other points. This case renders the simplifying assumptions of Ohm's law invalid and necessitates a more generic approach based on the Boltzmann equation.

To illustrate the aforementioned arguments, let us first consider a simplified structure of a semi-infinite slab of GRs. The height is taken to be infinite so that the z-dimensionality can safely be excluded from any consideration, whereas the width is kept semi-infinite to simplify the explanations yet not miss the vital points. In Fig. 3, the carrier transport mechanism in GR is explained.

In the following paragraphs, we start from the basic Boltzmann equation and highlight the condition under which Ohm's law is valid and subsequently, in the next section, prove that this condition is not satisfied by GRs at high frequencies. Note that all equations that will be developed correspond to the electrons. However, because holes involve only sign changes and the final result remains unaltered, the model is equally valid, irrespective of whether electrons or holes are the majority carriers. Now, the distribution function for carriers is given by

$$f = f_0 + f_1(\boldsymbol{v}, \boldsymbol{r}) \quad f_0 = \left(1 + \exp\frac{E - E_f}{K_B T}\right)^{-1} \tag{1}$$

where f_0 and f_1 are the equilibrium and nonequilibrium distribution functions, respectively, $\boldsymbol{v}$ is the velocity vector, $\boldsymbol{r}$ is the space vector, E_f is the Fermi level, K_B is the Boltzmann's constant, and T is the temperature. The Boltzmann equation for the distribution function of the conduction electrons is given by

$$\boldsymbol{v}.\nabla_{\boldsymbol{r}} f + \frac{(1 + i\omega\tau)}{\tau} f_1 = \frac{e}{\hbar}\boldsymbol{\varepsilon}.\nabla_{\boldsymbol{k}} f \tag{2a}$$

Here, $\boldsymbol{\varepsilon}$ and $\boldsymbol{k}$ are the electric-field and wave vectors, respectively, τ is the momentum relaxation time, ω is the angular frequency, e is the electronic charge, and $\hbar = h/2\pi$ where h is the Planck's constant. The electric field and the distribution function do not vary along the transport direction, i.e., y. Hence, $\partial f/\partial y$ reduces to zero. Moreover, because the dimension along z-direction is considered infinite, and $\partial f/\partial z$ is negligible. Thus, the $\boldsymbol{v}.\nabla_{\boldsymbol{r}} f$ term in (2a) reduces to $v_x(\partial f/\partial x)$. Because the electric field is applied along the y-direction, only the y-directed term remains in the right-hand side (RHS) of (2a). Hence, the 3-D Boltzmann equation reduces to

$$v_x \frac{\partial f}{\partial x} + \frac{(1 + i\omega\tau)}{\tau} f_1 = \frac{e}{\hbar}\varepsilon(x)\frac{\partial f}{\partial k_y}. \tag{2b}$$

Here, v_x represents the component of velocity along the x-axis, and $\varepsilon(x)$ is the y-directed electric field, which is a function of x. If we assume that the first term on the left hand side in (2b) can be neglected, we obtain the well-known Ohm's law, and the equation for current density is given by (3) (readers are referred to [14] for details of the derivation method)

$$J(x) = \frac{\sigma_{\mathrm{dc}}\varepsilon(x)}{1 + i\omega\tau} \tag{3}$$

where σ_{dc} is the dc conductivity.

Now, before we discuss the condition under which the assumption made to derive Ohm's law is valid, we require a small discussion on the skin depth. For calculating the skin depth, first Maxwell's equations given by (4a) can be used to relate the electric field to the current density [see (4b)] by eliminating magnetic-field terms and neglecting the displacement current

$$\nabla \times \boldsymbol{H_0} = \boldsymbol{J} + \frac{\partial \boldsymbol{D}}{\partial t} \quad \nabla \times \boldsymbol{\varepsilon} = -\mu\frac{\partial \boldsymbol{H_0}}{\partial t} \tag{4a}$$

$$\frac{\partial^2 \varepsilon(x)}{\partial x^2} = i\mu_0\omega J(x) \quad \mu_0 = 4\pi \times 10^{-7} \tag{4b}$$

where $\boldsymbol{J}$ is the current density, $\boldsymbol{D}$ is the electric displacement field, and μ is the permeability. The magnetic-field intensity is denoted by $\boldsymbol{H_0}$ to distinguish it from the height of the GR structure, which is represented by H.

Based on (3) and (4b), we can eliminate the current density term and the electric field can be solved as

$$\varepsilon(x) = \varepsilon(0)\exp\left\{-\frac{(1+i)x}{\delta'\sqrt{(1+i\omega\tau)}}\right\} \text{ where } \delta' = \sqrt{\frac{2}{\omega\mu_0\sigma}}. \tag{5}$$

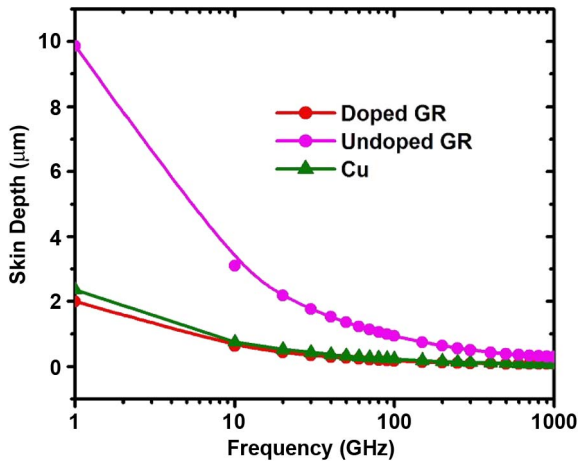

Fig. 4. Variation of skin depth with frequency for Cu, undoped GR, and doped GR. The values of σ and τ for Cu and GRs used to plot the graphs are discussed in details in Section II-B.

Then, the skin depth can be derived from (5) as

$$\delta = \delta' \sqrt{[1+(\omega\tau)^2] * \left[\sqrt{1+(\omega\tau)^2} - \omega\tau\right]} \qquad (6)$$

At low frequencies, the kinetic inductance (KI) term $\omega\tau$ can be neglected, and hence, $\delta \approx \delta'$.

Fig. 4 shows the variation of skin depth with frequency. The skin depth decreases as frequency is increased. Due to its lower conductivity value, the skin depth of the undoped GR is found to be much larger compared to Cu or doped GR.

It can be proven that the first term in (2b) can be neglected when the condition $l/\delta' \ll (1+\omega^2\tau^2)^{3/4}$ is satisfied [12]. Here, l is the MFP given by $l = v_f\tau$, where v_f is the Fermi velocity. Now, when the condition is not satisfied, Ohm's law becomes invalid, and ASE creeps in. We call the ratio $l/\delta' * (1+\omega^2\tau^2)^{-(3/4)}$ the critical ratio (CR). If the KI is neglected, the CR becomes simply l/δ'. We can say that ASE becomes important when CR approaches unity.

B. ASE: GR Versus Cu and CNT

In the following discussion, we show why ASE is an issue at high frequencies in GRs but is not very critical for other interconnect materials such as Cu and CNTs.

In Fig. 5(a) and (b), CR without and with the KI is plotted for undoped GR, doped GR, and Cu. VLSI Cu is considered, because even for the wide global wires, the conductivity corresponds to that of the VLSI Cu, which is 0.4545 $(\mu\Omega\cdot\text{cm})^{-1}$ [15]. The lower conductivity of VLSI Cu compared to the bulk Cu is mainly due to grain boundary and surface scattering as well as the presence of a barrier layer. The values of v_f and τ for Cu are 1.57×10^6 m/s and 2.5477×10^{-14} s, respectively, [16]. The Fermi velocity of GR is given as $v_f = \sqrt{3}\pi\gamma a/h$, where $\gamma = 3$ eV is the overlap integral between nearest neighbor π orbitals, and $a = 0.246$ nm is the lattice constant [17]. To obtain the value of τ, we use the values of MFP that have been extracted from the experimental results of bulk graphite in [1], which takes into account the impact of layer-to-layer interactions that reduce the conductivity in multilayered GRs. For a neutral GR with an in-plane conductivity of 0.026 $(\mu\Omega\cdot\text{cm})^{-1}$ [18], layer spacing of 0.34 nm, and $E_f = 0$, MFP is extracted to be 419 nm, whereas for the stage-2 AsF_5 intercalated graphite with a hole volume concentration (n_p) of 4.6×10^{20} cm^{-3}, the in-plane conductivity of 0.63 $(\mu\Omega\cdot\text{cm})^{-1}$, average layer spacing (s) between two adjacent graphene layers of 0.575 nm, and $|E_f| = 0.60$ eV, MFP is extracted to be 1.03 μm. In [1], MFP is defined as $l_d = v_f\tau_b$, where τ_b is the backscattering time, which corresponds to the relaxation of momentum from P to $-P$ and can be related to the momentum relaxation time τ (corresponding to the relaxation from P to 0) as $\tau_b = 2\tau$. Thus, τ can be written as $\tau = (l_d/2v_f)$. The curves with KI show a peak with decay at both ends, but no such effect is observed in the plot without KI. The increase in CR at lower frequencies can be attributed to the decrease in skin depth, as shown in Fig. 4. However, at very high frequencies, KI dominates and causes the CR to again reduce due to the increase in the $\omega\tau$ term. It is shown that the CR in doped GR increases much more rapidly compared to that of Cu, and this is because of the large MFP of GR. It is clear from the graphs that CR in Cu tends to one only at very high frequencies, whereas in doped GR, it cannot be neglected compared to one, even around 1 GHz. Thus, ASE needs to be considered for GR, even at much lower frequency ranges, whereas it will not be an issue in traditional metals such as Cu, except at very high frequencies ($>$ 100 GHz). As we move toward even higher frequencies, the CR in doped GR is shown to rapidly decay due to its larger KI [see Fig. 5(b)]. ASE will not be a serious issue in undoped GR because of its smaller MFP and higher resistivity. Because monolayer GR has extremely high resistance, it will also not be susceptible to ASE.

Readers may be inclined to think that CNT structures, which also enjoy a large MFP, should also be susceptible to ASE. However, it is not the case, as explained in the following discussion. In CNT bundles (see Fig. 6), the transport is 1-D, i.e., along the axis of the CNT, which is direction y in the figure, and only the MFP along this direction is large. The impedance from one CNT to another, i.e., the impedance in both x- and z-directions is very high, and thus, the MFP in these two directions is very small. Thus, any electric field and current distributions that take place along these directions have length scales that are much larger than the MFP within the frequency range of interest, and hence, ASE is not an issue in CNTs. Graphene, on the other hand, has large MFP not only in the transport direction, i.e., y, but also along x (see Fig. 3), and hence, the distributions along the x-direction will be influenced by ASE. The layer-to-layer impedance in multilayer GRs is very high, and hence, there is no ASE in the z-direction.

Thus, the high-frequency analysis of GRs is much more involved compared to CNTs or traditional metals. The impedance extraction method developed for CNTs [8] is not applicable to GRs. A thorough quantitative analysis is required to accurately evaluate the high-frequency effects in GRs, with detailed investigation into the skin effects, but to the best of our knowledge, there is no report in the literature to this end. In this paper, for the first time, a rigorous investigation is carried out into the intricate high-frequency processes in GR structures,

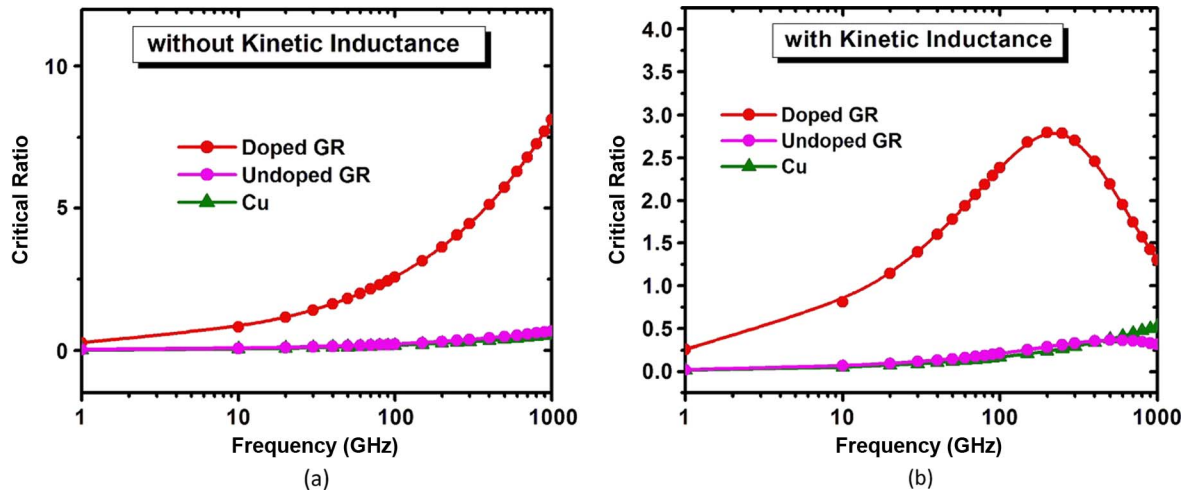

Fig. 5. Variation of critical ratio with frequency for Cu, undoped GR, and doped GR (a) without and (b) with consideration of kinetic inductance.

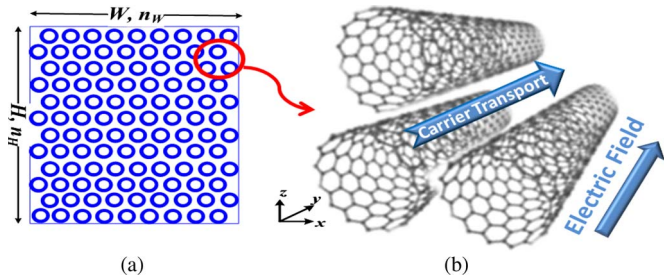

Fig. 6. (a) Cross-sectional view of a CNT bundle with width W and height H. n_W and n_H are the number of CNTs along the width and height, respectively. (b) Carrier transport in CNT. In CNT bundles, the carriers move only in one direction, i.e., along y, which is the direction of axis of the CNTs. Carrier transport from one tube to another, i.e., along the x- and z-directions, is negligible because of the high impedance between the tubes. Thus, the MFPs along these two directions are also small.

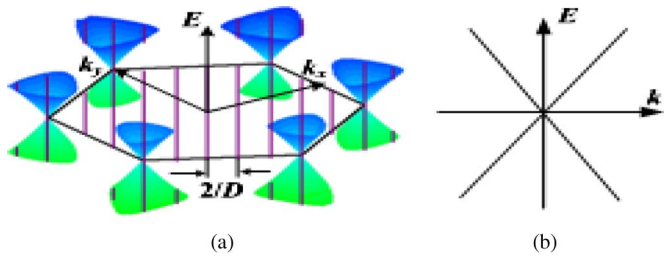

Fig. 7. (a) Two-dimensional hexagonal Brillouin zone (BZ) of graphene. Dirac cones are located at the six corners of the BZ. (b) Linear *E–k* relation of graphene near the Dirac points.

and an accurate methodology is developed by considering all of the important effects. The developed model not only provides accurate evaluation of impedance at high frequencies but is also equally efficient at lower frequencies and in the calculation of exact values of the dc resistance.

III. Impedance Modeling of GR

A. Semi-Infinite Slab

Because the condition for Ohm's law is not valid for GRs at high frequencies, we need to derive the current density for GRs without the simplifying assumption of Ohm's law. This approach is what we will implement in this section for a semi-infinite slab of GRs, and subsequently, using the derived current density, we show the calculation of the surface impedance.

Derivation of Current Density: As has been explained in the previous section, the x derivative of f cannot be neglected in the case of GRs. Hence, to accurately extract the impedance, we solve (2b), retaining all the terms. We can write

$$\frac{\partial f}{\partial k_y} \approx \frac{\partial f_0}{\partial E}\frac{\partial E}{\partial k}\frac{\partial k}{\partial k_y}.$$

We use the linear dispersion relation of graphene (as shown in Fig. 7 [19]) as

$$E = \hbar v_f k \tag{7a}$$
$$v_x = v_f \cos\theta \tag{7b}$$
$$v_y = v_f \sin\theta. \tag{7c}$$

The angle θ is defined in Fig. 3(b). We can assume $(\partial f/\partial x) \approx (\partial f_1/\partial x)$ since the variation of the equilibrium function (f_0) with x i.e., $\partial f_0/\partial x$ is negligible compared to that of the non-equilibrium function (f_1) i.e., $\partial f_1/\partial x$. Now, using (7) and $\partial k/\partial k_y = \sin\theta$, we finally obtain the following equation:

$$v_x\frac{\partial f_1}{\partial x} + \frac{(1+i\omega\tau)}{\tau}f_1 = ev_y\varepsilon(x)\frac{\partial f_0}{\partial E}. \tag{8}$$

The general solution to the differential equation given by (8) is

$$f_1 = \exp\left(-\frac{(1+i\omega\tau)x}{\tau v_x}\right) \times \left\{F(v) + \frac{e}{v_x}\frac{\partial f_0}{\partial E}\int_0^x v_y\varepsilon(t)\exp\left(\frac{(1+i\omega\tau)t}{\tau v_x}\right)dt\right\} \tag{9}$$

where $F(v)$ is a function of velocity v, which can be solved from the boundary conditions. The inclusion of electric field within the integral takes into account that the distribution function at any point is not a local function of the electric field at that point but also includes other points, which is absolutely essential for the treatment of ASE. The boundary condition for

$v_x < 0$ can be derived from the fact that f_1 should not become exponentially large as $x \to \infty$ [12], and hence, we get

$$f_1^- = -\frac{e}{v_x}\frac{\partial f_0}{\partial E}\int_x^\infty v_y \varepsilon(t,z)\exp\left(-\frac{(1+i\omega\tau)(x-t)}{\tau v_x}\right)dt. \quad (10)$$

f_1^- is the distribution function for $v_x < 0$. The boundary condition for $v_x > 0$ depends on the edge scattering. For our analysis, we have considered the two extreme cases of perfectly diffuse ($p = 0$) and perfectly specular ($p = 1$) reflection, where p is the fraction of carriers elastically scattered at the edges. For diffuse reflection, the drift velocity is reduced to zero after scattering at the edge, whereas in the case of specular reflection, complete reversal of drift velocity occurs. Thus, the boundary conditions for the two cases are given by

$$f_1^+(v, x=0) = 0 \quad \text{for } p = 0 \quad (11a)$$

$$f_1^+(v_x, v_y, v_z, x=0) = f_1^-(-v_x, v_y, v_z, x=0) \quad \text{for } p = 1 \quad (11b)$$

where f_1^+ is the distribution function for $v_x > 0$, and $x = 0$ denotes an edge of the GR structure. Based on the aforementioned boundary conditions, we arrive at

$$f_1^+ = \frac{e}{v_x}\frac{\partial f_0}{\partial E}\int_0^x v_y\varepsilon(t,z) \times \exp\left(-\frac{(1+i\omega\tau)(x-t)}{\tau v_x}\right)dt \quad for\ p=0 \quad (12a)$$

$$= \frac{e}{v_x}\frac{\partial f_0}{\partial E}\int_{-\infty}^x v_y\varepsilon(t,z) \times \exp\left(-\frac{(1+i\omega\tau)(x-t)}{\tau v_x}\right)dt \quad for\ p=1. \quad (12b)$$

In graphene, the current transport is 2-D within a layer. The 2-D current density is given by

$$J_{2D} = -\sum_i en\langle v_y\rangle \quad (13a)$$

where n is the 2-D density of carriers, $\langle v_y\rangle$ is the ensemble average over the distribution function f, and the summation is over all the valleys indexed by i in the Brillouin zone (BZ). Expanding the expression for $\langle v_y\rangle$, (13a) becomes

$$J_{2D} = -\frac{2en\int v_y f dk\, 2(L/2\pi)^2}{\int f dk\, 2(L/2\pi)^2}. \quad (13b)$$

The prefactor of 2 in the aforementioned equation corresponds to the two equivalent valleys of graphene, which has a hexagonal BZ (see Fig. 7), with each vertex contributing 1/3 of a valley. The 3-D current density can be obtained by multiplying by the number of layers N_l and dividing by the height. Thus, we get

$$J = J_{2D} * N_l/H = J_{2D}/s \quad (13c)$$

where s is the average spacing between the layers. Equation (13c) can be simplified and written as

$$J(x) = -\frac{e}{\pi^2 s}\int v_y f_1 dk. \quad (13d)$$

Substituting the expression for f_1 based on (10) and (12) and solving (13d) using (7), the current density can be expressed as

$$J(x) = \frac{2e^2E_f}{\pi^2\hbar^2 v_f s}\int_0^\infty g\left(\frac{x-t}{l}\right)\varepsilon(t)\,dt \quad \text{for } p=0 \quad (14a)$$

$$= \frac{2e^2E_f}{\pi^2\hbar^2 v_f s}\int_{-\infty}^\infty g\left(\frac{x-t}{l}\right)\varepsilon(t)dt \quad \text{for } p=1 \quad (14b)$$

where

$$g(u) = \int_0^{\pi/2}\frac{\sin^2\theta}{\cos\theta}\exp\left\{\frac{(1+i\omega\tau)|u|}{l\cos\theta}\right\}d\theta.$$

Detailed derivation of (14) based on (13d) is shown in the Appendix.

Calculation of the Surface Impedance: Now, using (4b) and substituting $u_1 = x/l$, $u_2 = t/l$ and defining the function $\xi(u_1) = \varepsilon(lu_1)$, we get

$$\xi''(u_1) = i\alpha\left\{p\int_{-\infty}^\infty g(u_1-u_2)\xi(u_2)\,du_2 + (1-p)\int_0^\infty g(u_1-u_2)\xi(u_2)\,du_2\right\} \quad (15)$$

where $\alpha = (2e^2E_f l^3\mu_0\omega/\pi^2\hbar^2 v_f s)$.

Now, the surface impedance (at $x = 0$) can be calculated as $Z_S = (\varepsilon(0)/\int_0^\infty J(x)dx)$, and using (4b), we get

$$Z_S = -i\mu_0\omega\frac{\varepsilon(0)}{\varepsilon'(0)} \quad (16)$$

which can also be written as

$$Z_S = -i\mu_0\omega l\frac{\xi(0)}{\xi'(0)}. \quad (17)$$

$(\xi(0)/\xi'(0))$ can be calculated from (15) by standard methods based on the theory of Fourier integrals. Readers are referred to [12] for details of the calculation method.

If the normal skin effect (NSE) and Ohm's law were valid, the surface impedance could be calculated from (5) and (16) as

$$Z_S = \sqrt{\frac{\omega\mu_0}{2\sigma}}\left\{\sqrt{\sqrt{(\omega\tau)^2+1}-\omega\tau} + i\sqrt{\sqrt{(\omega\tau)^2+1}+\omega\tau}\right\}. \quad (18)$$

Fig. 8(a) shows the variation of surface resistance with frequency for both $p = 0$ and $p = 1$, where ASE is taken into account, and the results are compared with the case of NSE. KI is neglected here for simplifying the current problem, because here, we are mainly interested in comparing NSE and ASE. We show the effect of KI in the more rigorous analysis of finite GR structures in the companion paper (part II) [20]. It can be observed that, at lower frequencies, all the curves merge together. However, at higher frequencies, the increase in resistance with ASE taken into account (for both $p = 0$ and $p = 1$) is greater than the case where ASE is neglected (i.e.,

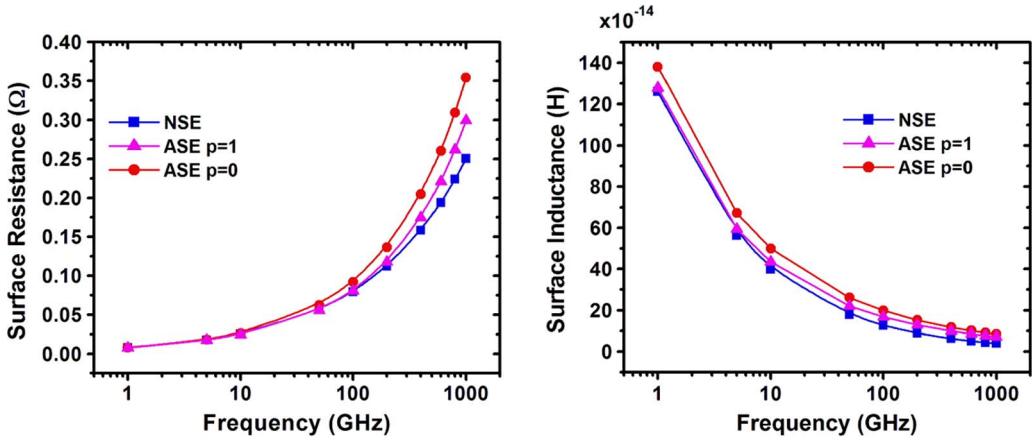

Fig. 8. (a) Surface resistance and (b) surface inductance of a semi-infinite slab of GR as a function of frequency.

NSE) and the difference increases with frequency. Another important point to note is that the resistance for $p = 0$ is higher than at $p = 1$, and the difference between the two also increases as frequency is increased. The variation of surface inductance with frequency is plotted in Fig. 8(b). The surface inductance decreases as frequency is increased, because with the increase in frequency, the current gets confined much more toward the edges. In addition, the effect of ASE for $p = 0$ is found to be more compared to that for $p = 1$. A detailed discussion on these effects can be found in the companion paper [20].

B. Practical Structures

The GR structures relevant for high-frequency interconnect and inductor designs have finite rectangular cross sections. The dimensions chosen here are relevant for top global interconnects and high-frequency inductor design. Very small dimensions (W $<$ 10 nm) will show worse performance, as already pointed out in [1], and hence are not considered in this paper. Second, there is no impact of skin effect when the dimensions are very small. Hence, the effective conductivity at high frequencies would be the same as the dc conductivity, the analysis of which has been done in previous literature [1]. For practical GRs, the electric field and current distribution will be a function of both x- and z-directions, hence, (15) and the aforementioned standard procedure for the calculation of the impedance will not be valid here. Therefore, in this section, we present a model for calculating the impedance of finite GR structures. First, we present a generic approach, which is valid at all frequencies, followed by a simplified model, which may be adopted at relatively lower frequencies.

Generic Approach: Although, now, the height is finite, $v_z(\partial f/\partial z)$ can still be neglected, because the velocity along the z-direction is negligible. Hence, the 3-D Boltzmann equation basically reduces to the same form as in (8), and the distribution function can be expressed by (9), with the only exception that, in both the equations and in all subsequent equations, the electric field is a function of both x and z. The boundary conditions for solving $F(v)$ are given by

$$\text{for } p = 0$$
$$f_1^+(v, x = 0) = 0 \tag{19a}$$
$$f_1^-(v, x = W) = 0 \tag{19b}$$
$$\text{for } p = 1$$
$$f_1^+(v_x, v_y, v_z, x = 0) = f_1^-(-v_x, v_y, v_z, x = 0) \tag{19c}$$
$$f_1^+(-v_x, v_y, v_z, x = W) = f_1^-(v_x, v_y, v_z, x = W). \tag{19d}$$

Based on the aforementioned boundary conditions, f_1 can be solved as

$$\text{for } p = 0$$
$$f_1^+ = \frac{e}{v_x}\frac{\partial f_0}{\partial E}\int_0^x v_y \varepsilon(t,z) \times \exp\left(-\frac{(1+i\omega\tau)(x-t)}{\tau v_x}\right) dt \tag{20a}$$
$$f_1^- = -\frac{e}{v_x}\frac{\partial f_0}{\partial E}\int_x^W v_y \varepsilon(t,z) \times \exp\left(-\frac{(1+i\omega\tau)(x-t)}{\tau v_x}\right) dt \tag{20b}$$
$$\text{for } p = 1$$
$$f_1^+ = f_1^- = \frac{e}{v_x}\frac{\partial f_0}{\partial E} \times \int_0^W \frac{v_y \varepsilon(t,z)}{\exp\left(\frac{(1+i\omega\tau)W}{\tau v_x}\right) - \exp\left(-\frac{(1+i\omega\tau)W}{\tau v_x}\right)} * \left[\exp\left(-\frac{(1+i\omega\tau)(-W+x+t)}{\tau v_x}\right) + \exp\left(-\frac{(1+i\omega\tau)(W+x-t)}{\tau v_x}\right)\right] dt + \frac{e}{v_x}\frac{\partial f_0}{\partial E}\int_0^x v_y \varepsilon(t,z) \times \exp\left(-\frac{(1+i\omega\tau)(x-t)}{\tau v_x}\right) dt. \tag{20c}$$

Now, incorporating the expression for f_1 based on (20) in (13d), the current density $J(x, z)$ across the GR structure is calculated through numerical integration, with an initial guess of the electric field. Then, Green's function approach is used

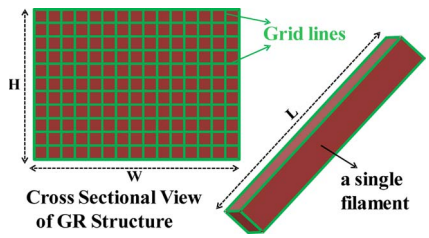

Fig. 9. Division of the GR structure into small filaments for applying Green's function.

to calculate the new electric-field distribution as explained in the following discussion. For this purpose, the GR structure is divided into several small filaments, as shown in Fig. 9. Self and mutual inductances are calculated for the filaments from which Green's function is derived. The self inductance per unit length ($L_{\rm Self}$, in microhenry per meter) of a filament is given by [21]

$$L_{\rm Self} = 0.2\left[\ln(2L/{\rm GMD}) - 1.25 + {\rm AMD}/L + (\mu/4)T\right]. \quad (21)$$

Here, L is the length, GMD and AMD are the geometric and arithmetic mean distances, respectively, for a single filament, μ is the permeability, and T is the frequency-correction parameter, which equals 1 for a near-direct-current condition. The division of the GR structure is done in such a way that each filament has a square cross section, and the GMD for each single filament is given by 0.44705 times the side of a filament [21]. AMD, in this case, is defined as the average of all possible distances within a cross section of a filament, and it is numerically calculated.

Mutual inductance between different filaments can be calculated from the following equations:

$$Q_{\rm jk} = \ln\left\{(L/d_{\rm jk}) + \left[1 + \left(L^2/d_{\rm jk}^2\right)\right]^{1/2}\right\} - \left[1 + \left(d_{\rm jk}^2/L^2\right)\right]^{1/2} + (d_{\rm jk}/L) \quad (22a)$$

$$M_{\rm jk} = 0.2 Q_{\rm jk}. \quad (22b)$$

Here, $Q_{\rm jk}$ is the mutual inductance parameter, $M_{\rm jk}$ is the mutual inductance per unit length (in microhenry per meter), and $d_{\rm jk}$ is the distance between the centers of the two filaments considered, respectively. Note that the more accurate equation requires $d_{\rm jk}$ substituted by $GMD_{\rm jk}$, i.e., the geometric mean distance between the jth and kth filaments. However, because $GMD_{\rm jk}$ is almost equal to $d_{\rm jk}$, we will use $d_{\rm jk}$ for simplicity. Green's function is given by

$$G_{\rm jk} = L_{\rm self} \quad \text{if } j = k$$
$$= M_{\rm jk} \quad \text{otherwise.} \quad (23)$$

The vector potential is calculated as

$$A_j = a_f \sum_k G_{\rm jk} J_k. \quad (24)$$

Here, a_f is the cross-sectional area of a filament. The current and electric field in each filament is approximated by the values at the center of the respective filament, and J_k represents the current density at the center of the kth filament.

The voltage drop across a filament j can be expressed as

$$V_j = (\varepsilon_j + i\omega A_j)L. \quad (25)$$

Because we are working with an initial guessed value of electric field, the voltage drop across different filaments may be different. The average voltage drop $V_{\rm avg}$ is calculated, and a new value of electric-field distribution is obtained from it. All the steps are then repeated with the new values of electric field, and iterations are continued until convergence is separately achieved for both the real and imaginary parts of the electric field. Finally, based on this self-consistent procedure, the impedance is obtained as

$$Z = \frac{V_{\rm avg}}{a_f \sum_k J_k}. \quad (26)$$

Simplified Methodology: The aforementioned methodology is a very generic approach. However, when the MFP is much smaller compared to the skin depth or at lower frequencies, only NSE occurs, and some simplifying assumptions can be adopted for such cases. Ohm's law remains valid, and the current density at any point can be assumed to depend only on the value of the electric field at that same point. Thus, in the equation for the nonequilibrium distribution function [see (9)], the electric field can be taken out of the integration, and this approach results in much simplified expressions for f_1. We have

$$f_1^+(v,x) = e\tau v_y \varepsilon \frac{\partial f_0}{\partial E} \times \left\{1 - (1-p)\left(1 - p\exp\left(-\frac{W}{\tau v_x}\right)\right)^{-1} \times \exp\left(-\frac{x}{\tau v_x}\right)\right\} \quad (27a)$$

$$f_1^-(v,x) = e\tau v_y \varepsilon \frac{\partial f_0}{\partial E} \times \left\{1 - (1-p)\left(1 - p\exp\left(\frac{W}{\tau v_x}\right)\right)^{-1} \times \exp\left(\frac{W-x}{\tau v_x}\right)\right\}. \quad (27b)$$

The KI term has intentionally been dropped in the aforementioned equations, and it is taken into account at a later stage, as would be clear from the explanations in the following passages. To take the size effects into account, effective conductivity is extracted. For this purpose, the dc current density [see (28a)] is first calculated from the Boltzmann distribution function given by (27). Then, the average current density is evaluated and is used to find the effective dc conductivity $\sigma_{\rm eff\_dc}$, which is shown in (28b). Note that, in (28a), the current density is only a function of the x-direction and not of z, because the electric field is considered constant here. Because, here, we are interested only in the calculation of $\sigma_{\rm eff\_dc}$, the electric field

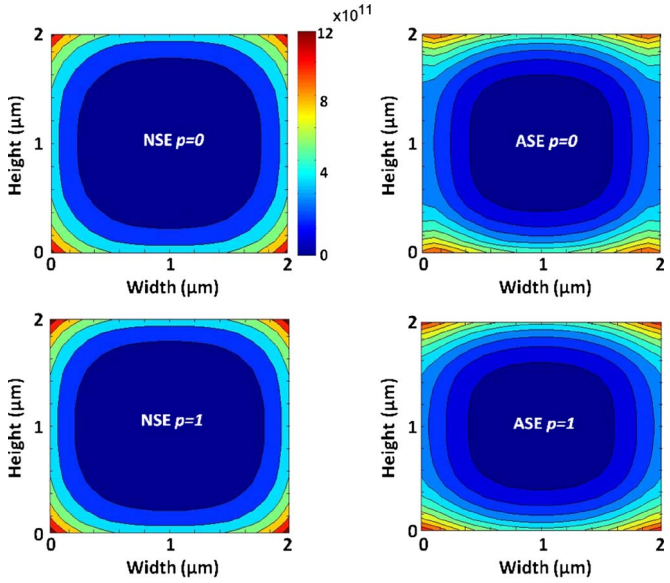

Fig. 10. Normalized current density distribution graphs across the cross section of a 2×2 μm^2 GR structure. The color scale shown is the same for all the distribution plots.

has no actual role to play, and it gets cancelled in (28b); hence, we could also have effectively replaced it by 1. We have

$$J_{dc}(x) = -\frac{e}{\pi^2 s}\iint v_y f_1 k \partial k \partial\theta \tag{28a}$$

$$\sigma_{\text{eff\_}dc} = \frac{1}{W\varepsilon}\int_0^W J(x)\partial x. \tag{28b}$$

Now, the momentum relaxation time is updated to include the size effects, and we obtain the effective momentum relaxation time τ_{eff} as shown in (29a). Finally, the KI term is incorporated, and the effective ac conductivity σ_{eff} is obtained as in (29b)

$$\tau_{\text{eff}} = \frac{\sigma_{\text{eff\_}dc}}{\sigma_0}\tau \tag{29a}$$

$$\sigma_{\text{eff}} = \frac{\sigma_{\text{eff\_}dc}}{1 + i\omega\tau_{\text{eff}}}. \tag{29b}$$

The current density can be expressed as

$$J(x,z) = \sigma_{\text{eff}}\varepsilon(x,z). \tag{30}$$

The current density distribution within the GR structure can be calculated from (30), starting with an initial guess of electric-field distribution. Then, the self-consistent iteration method described for ASE is followed for the calculation of the impedance.

High-Frequency Analysis: The normalized current density distribution plots across the cross section of a 2×2 μm^2 GR structure are shown in Fig. 10. It is observed that, when only NSE is considered, current density J is symmetrical about x and z (the distribution remains the same if the plot is rotated by 90°) and no visible difference is obtained between $p = 0$ and $p = 1$. Meanwhile, in the case of ASE, the contours take on a different shape about x and z, as well as between $p = 0$ and $p = 1$. To explain the aforementioned results, we need to take into account two important effects. First, the skin effect tends to confine the current toward the boundaries. However, near the boundaries $x = 0$ and $x = W$ (which are the edges of the GR layers), the edge-scattering effect causes reduction in the current density compared to that at $z = 0$ and $z = H$ (which are the bottom and top GR layers, respectively). Hence, we get the asymmetrical distribution in the case of ASE. On the other hand, NSE gives symmetrical contours, because it is obtained using Ohm's law with an effective conductivity. In addition, between the two edge specularities, $p = 0$ results in the lowest current density, because it is related to completely diffusive scattering, and this effect can be observed only when ASE is taken into account. Thus, the impact of the edge-scattering effect can only be appreciated when ASE is considered. It can also be noted that NSE leads to higher estimation of current density compared to ASE.

In Fig. 11, the resistance and inductance of the GR structure, considering ASE, is plotted as a function of frequency for both $p = 0$ and $p = 1$. Edge specularity is found to have considerable impact on the resistance, whereas its effect on the inductance is found to be almost negligible. Detailed analysis of the effect of edge scattering and ASE is reported in the companion paper [20].

IV. Conclusion

An accurate model has been developed in this paper for the extraction of high-frequency impedance of GR interconnects. The methodology presented is generic in the sense that it can be used not only for the evaluation of high-frequency impedance but also for the accurate extraction of low-frequency and dc impedance. Using the Boltzmann equation coupled with the E–k relation for graphene, the current density in a GR structure is derived, taking into account the nonlocal values of electric field. Then, the electric field and current density is self consistently calculated using the magnetic vector potential Green's function approach. It is shown that, to accurately obtain the current density distribution and, consequently, the impedance, ASE should be taken into account. The proposed methodology can be used to analyze the high-frequency effects in multilayered GRs and investigate the important implications for high-frequency applications such as in VLSI interconnects and inductor design, as discussed in the companion paper.

Appendix A

Based on (10), (12a), and (13d), we can write for $p = 0$

$$J(x) = -\frac{e^2}{\pi^2 s} \times \left\{ \int_0^x dt \int_{v_x>0} \frac{v_y^2}{v_x}\varepsilon(t)\exp\left(-\frac{(1+i\omega\tau)(x-t)}{\tau v_x}\right) \times \frac{\partial f_0}{\partial E}dk - \int_x^\infty dt \int_{v_x<0} \frac{v_y^2}{v_x}\varepsilon(t) \times \exp\left(-\frac{(1+i\omega\tau)(x-t)}{\tau v_x}\right)\frac{\partial f_0}{\partial E}dk \right\}. \tag{A1}$$

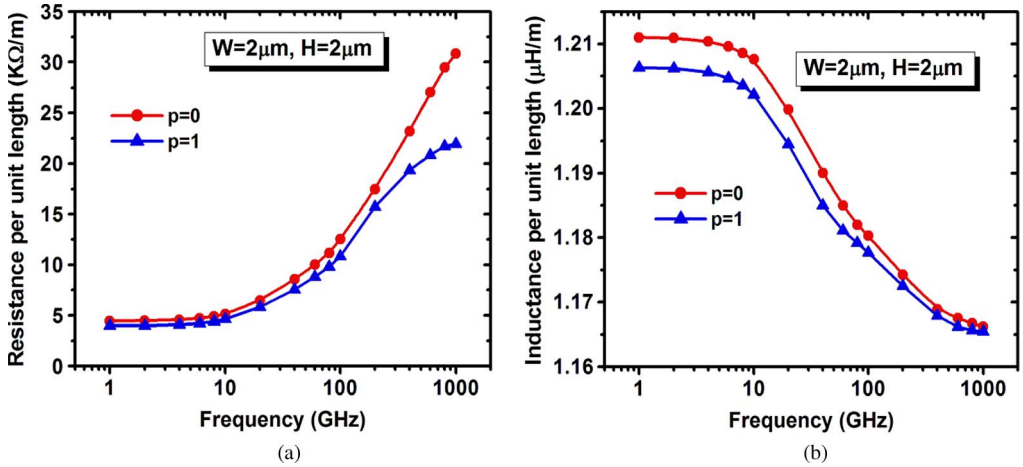

Fig. 11. Variation of the (a) resistance and (b) inductance of GR structure with frequency for both $p = 0$ and $p = 1$. L is taken to be 500 μm.

Let us represent the integral over $\mathbf{k}$ for $v_x > 0$ as I_1 and that for $v_x < 0$ as I_2. Thus, (A1) can be written as

$$J(x) = -\frac{e^2}{\pi^2 s}\left\{\int_0^x dt I_1 - \int_x^\infty dt I_2\right\}. \quad \text{(A2)}$$

Now, using (7b) and (7c), we get

$$I_1 = \int_0^\infty \int_{-\pi/2}^{\pi/2} \frac{(v_f \sin\theta)^2}{v_f \cos\theta}\varepsilon(t) \times \exp\left(-\frac{(1+i\omega\tau)(x-t)}{\tau v_f \cos\theta}\right)\frac{\partial f_0}{\partial E} k dk d\theta. \quad \text{(A3)}$$

For doped GR, we can write $(\partial f_0/\partial E) \approx -\delta(E - E_f)$, and using (7a), we obtain

$$I_1 = -\frac{2E_f}{\hbar^2 v_f}\int_0^{\pi/2} \frac{(\sin\theta)^2}{\cos\theta}\varepsilon(t)\exp\left(-\frac{(1+i\omega\tau)(x-t)}{\tau v_f \cos\theta}\right)d\theta. \quad \text{(A4)}$$

Now, I_2 has basically the same form as in I_1, except that the θ integration is from $\pi/2$ to $3\pi/2$. Putting $\theta' = \pi - \theta$ and following the aforementioned similar steps for I_1, we get

$$I_2 = \frac{2E_f}{\hbar^2 v_f}\int_0^{\pi/2} \frac{(\sin\theta')^2}{\cos\theta'}\varepsilon(t)\exp\left(\frac{(1+i\omega\tau)(x-t)}{\tau v_f \cos\theta'}\right)d\theta'. \quad \text{(A5)}$$

Combining (A2), (A4), and (A5), the current density can be expressed as

$$J(x) = \frac{2e^2 E_f}{\pi^2\hbar^2 v_f s}\int_0^\infty \varepsilon(t)dt \int_0^{\pi/2} \frac{(\sin\theta)^2}{\cos\theta} \times \exp\left(-\frac{(1+i\omega\tau)|x-t|}{\tau v_f \cos\theta}\right)d\theta \quad \text{(A6)}$$

which is the same as (14a). Following a similar procedure, the current density for $p = 1$ can also be derived.

REFERENCES

[1] C. Xu, H. Li, and K. Banerjee, "Modeling, analysis, and design of graphene nanoribbon interconnects," *IEEE Trans. Electron Devices*, vol. 56, no. 8, pp. 1567–1578, Aug. 2009.

[2] Q. Shao, G. Liu, D. Teweldebrhan, and A. A. Balandin, "High-temperature quenching of electrical resistance in graphene interconnects," *Appl. Phys. Lett.*, vol. 92, no. 20, pp. 202 108-1–202 108-3, May 2008.

[3] A. Naeemi and J. D. Meindl, "Conductance modeling for graphene nanoribbon (GR) interconnects," *IEEE Electron Device Lett.*, vol. 28, no. 5, pp. 428–431, May 2007.

[4] A. Naeemi and J. D. Meindl, "Performance benchmarking for graphene nanoribbon, carbon nanotube, and Cu interconnects," in *Proc. IEEE Int. Interconnect Technol. Conf.*, San Francisco, 2008, pp. 183–185.

[5] A. A. Balandin, S. Ghosh, W. Bao, I. Calizo, D. Teweldebrhan, F. Miao, and C. N. Lau, "Superior thermal conductivity of single-layer graphene," *Nano Lett.*, vol. 8, no. 3, pp. 902–907, Feb. 2008.

[6] K. I. Bolotin, K. J. Sikes, J. Hone, H. L. Stormer, and P. Kim, "Temperature-dependent transport in suspended graphene," *Phys. Rev. Lett.*, vol. 101, no. 9, pp. 096 802-1–096 802-4, Aug. 2008.

[7] K. Banerjee, S. Im, and N. Srivastava, "Interconnect modeling and analysis in the nanometer era: Cu and beyond," in *Proc. Adv. Metallization Conf. (AMC)*, Colorado Springs, CO, Sep. 26–29, 2005.

[8] H. Li and K. Banerjee, "High-frequency analysis of carbon nanotube interconnects and implications for on-chip inductor design," *IEEE Trans. Electron Devices*, vol. 56, no. 10, pp. 2202–2214, Oct. 2009.

[9] L. R. Hanlon, E. R. Falardeau, and J. E. Fischer, "Metallic reflectance of AsF_5-graphite intercalation compounds," *Solid State Commun.*, vol. 24, no. 5, pp. 377–381, Nov. 1977.

[10] E. H. Sondheimer, "The mean free path of electrons in metals," *Adv. Phys.*, vol. 50, no. 6, pp. 499–537, Sep. 2001.

[11] E. H. Sondheimer, "The theory of anomalous skin effect in anisotropic metals," *Proc. R. Soc. Lond. A: Math. Phys. Sci.*, vol. 224, no. 1157, pp. 260–272, Jun. 1954.

[12] G. E. H. Reuter and E. H. Sondheimer, "The theory of the anomalous skin effect in metals," *Proc. R. Soc. Lond. A: Math. Phys. Sci.*, vol. 195, no. 1042, pp. 336–364, Dec. 1948.

[13] A. B. Pippard, "The surface impedance of superconductors and normal metals at high frequencies—Part II: The anomalous skin effect in normal metals," *Proc. R. Soc. Lond. A: Math. Phys. Sci.*, vol. 191, no. 1026, pp. 385–399, Nov. 1947.

[14] A. H. Wilson, *The Theory of Metals*. Cambridge, U.K.: Cambridge Univ. Press, 1936.

[15] Intl. Tech. Roadmap for Semiconductors (ITRS). [Online]. Available: http://public.itrs.net

[16] C. Kittel, *Introduction to Solid-State Physics*, 8th ed. Hoboken, NJ: Wiley, 2005.

[17] M. Dresselhaus, The Novel Nanostructures of Carbon: Univ. Tokyo Lecture, Jan. 2008. [Online]. Available: www.photon.t.u-tokyo.ac.jp/~maruyama/visitors/DresselhausPres.pdf

[18] L. X. Benedict, V. H. Crespi, S. G. Louie, and M. L. Cohen, "Static conductivity and superconductivity of carbon nanotubes—Relations between tubes and sheets," *Phys. Rev. B*, vol. 52, no. 20, pp. 14 935–14 940, Nov. 1995.

[19] H. Li, C. Xu, N. Srivastava, and K. Banerjee, "Carbon nanomaterials for next generation interconnects and passives: Physics, status and prospects," *IEEE Trans. Electron Devices*, vol. 56, no. 9, pp. 1799–1821, Sep. 2009.
[20] D. Sarkar, C. Xu, H. Li, and K. Banerjee, "High-frequency behavior of graphene-based interconnects—Part II: Impedance analysis and implications for inductor design," *IEEE Trans. Electron Devices*, vol. 58, no. 3, pp. 853–859, Mar. 2011.
[21] H. M. Greenhouse, "Design of planar rectangular microelectronic inductors," *IEEE Trans. Parts, Hybrids, Packag.*, vol. PHP-10, no. 2, pp. 101–109, Jun. 1974.

Deblina Sarkar (S'09) received the B.Tech. degree in electronics engineering from the Indian School of Mines University (ISMU), Dhanbad, India, in 2008. She is currently working toward the Ph.D. degree in Prof. Banerjee's Nanoelectronics Research Laboratory, Department of Electrical and Computer Engineering, University of California, Santa Barbara.

During the summer of 2007, she was an Intern with Prof. Laurens Molenkamp's Spintronics Group, Wurzburg University, Wurzburg, Germany. From November 2009 to February 2010, she was a Visiting Student Researcher with Infineon Technologies AG, Munich, Germany, and with the Interuniversity Microelectronics Centre, Leuven, Belgium. During the summer of 2010, she was a Visiting Student Researcher with the Institute of Microelectronics, Singapore. Her undergraduate research interests included novel nanoscale device design and spintronics. Her current research is focused on exploring carbon nanostructures and other novel materials for designing ultra energy-efficient electronics.

Ms. Sarkar was the recipient of the Best Paper Award at the Annual Paper Meet, Technical Fest, organized by the ISMU during her undergraduate study and the Best Female Student Award from the ISMU.

Chuan Xu (S'08) received the B.S. degree in microelectronics and the M.S. degree in microelectronics and solid-state electronics from the Institute of Microelectronics, Peking University, Beijing, China, in 2004 and 2007, respectively. He is currently working toward the Ph.D. degree in the Department of Electrical and Computer Engineering, University of California, Santa Barbara.

During his M.S. degree, he worked on the fabrication and characterization of AlGaN/GaN heterostructure field-effect transistors. In Fall 2007, he joined Prof. Banerjee's Group, Nanoelectronics Research Laboratory, University of California, Santa Barbara. His current research is focused on the modeling, design, and characterization of emerging interconnect materials, structures, and effects. During the summer of 2008, he was an Intern with the Electrical Interconnect and Packaging (EIP) Group, IBM T. J. Watson Research Center, Yorktown Heights, NY. During the summer of 2009 and 2010, he was an Intern with the Calibre Division, Mentor Graphics Corporation, St. Ismier, France.

Mr. Xu was the recipient of the 2008 IBM Problem Solving Award Based on the Use of the EIP Tool Suite, which recognizes outstanding contributions by students in solving the most interesting problems using the IBM electromagnetic field solver suite of tools called the EIP tools.

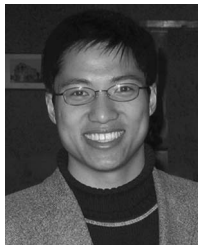

Hong Li (S'07) received the B.E. degree in electronic engineering from Nanjing University of Aeronautics and Astronautics, Nanjing, China, in 2003 and the M.S. degree from Shanghai Jiao Tong University, Shanghai, China, in 2008. He has been working toward the Ph.D. degree with Professor Banerjee's Group (Nanoelectronics Research Laboratory) in the Department Electrical and Computer Engineering, University of California, Santa Barbara (UCSB).

His research interests include the modeling, design, fabrication, and characterization of carbon nanomaterials for electronic applications, particularly VLSI interconnects and passive devices. Since December 2008, he has been the lead graduate student working on the development of a state-of-the-art carbon nanomaterial fabrication facility with the California Nanosystems Institute (CNSI), UCSB.

Mr. Li received a number of prizes for outstanding academic performance, including an Excellent Bachelor's Thesis Award, during his undergraduate years.

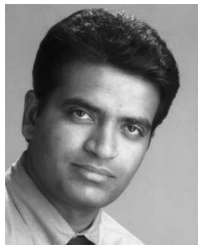

Kaustav Banerjee (S'92–M'99–SM'03) received the Ph.D. degree in electrical engineering and computer sciences from the University of California, Berkeley, in 1999.

From 1999 to 2001, he was a Research Associate with the Center for Integrated Systems, Stanford University, Stanford, CA. From February to August 2002, he was a Visiting Faculty with the Circuits Research Laboratories, Intel, Hillsboro, OR. He has also held summer/visiting positions with Texas Instruments Incorporated, Dallas, from 1993 to 1997 and with the Swiss Federal Institute of Technology, Lausanne, Switzerland, in 2001. Since July 2002, he has been with the faculty of the Department of Electrical and Computer Engineering, University of California, Santa Barbara (UCSB), where he has been a Full Professor since 2007. He is also an Affiliated Faculty with the California Nanosystems Institute and the Institute for Energy Efficiency, UCSB. His research has been chronicled in more than 200 journal articles and refereed international conference proceedings and in several book chapters. He is also a Coeditor of the book *Emerging Nanoelectronics: Life With and After CMOS* (Springer, 2004). His current research interests include nanometer-scale issues in VLSI, as well as circuits and system issues in emerging nanoelectronics. He is also involved in exploring the physics, technology, and applications of various carbon nanostructures for ultra-energy-efficient electronics and energy harvesting/storage applications.

Dr. Banerjee was the recipient of numerous awards in recognition of his work, including the Best Paper Award at the Design Automation Conference in 2001, the Association of Computing Machinery Special Interest Group on Design Automation Outstanding New Faculty Award in 2004, the IEEE Micro Top Picks Award in 2006, and an IBM Faculty Award in 2008. He has served on the Technical and Organizational Committees of several leading IEEE and ACM conferences, including the International Electron Devices Meeting, the Design Automation Conference, the International Conference on Computer-Aided Design, the International Reliability Physics Symposium, the International Symposium on Quality Electronic Design, the EOS/ESD Symposium, and the International Conference on Simulation of Semiconductor Processes and Devices. From 2005 to 2008, he served as a Member of the Nanotechnology Committee of the IEEE Electron Devices Society (EDS). He currently serves on the IEEE/EDS GOLD Committee and the IEEE/EDS VLSI Circuits and Technology Committee. He has been a Distinguished Lecturer of the IEEE Electron Devices Society since 2008.